Journal of Materials Chemistry A

Accepted Manuscript

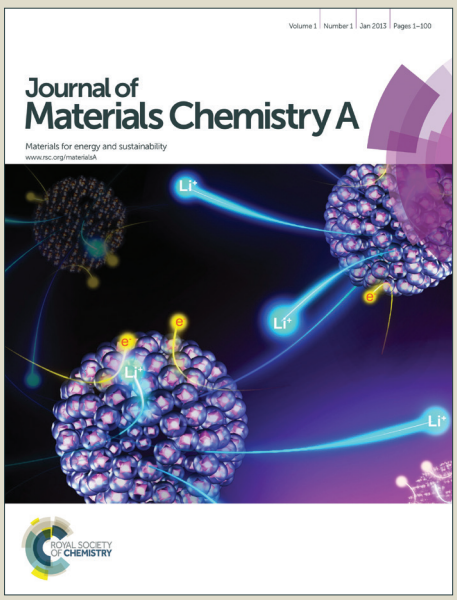

ROYAL SOCIETY OF CHEMISTRY

www.rsc.org/materialsA

Cite this: DOI: 10.1039/c0xx00000x

www.rsc.org/xxxxxx

ARTICLE TYPE

High thermoelectric performance of mechanically robust n-type $Bi_2Te_{3-x}Se_x$ prepared by combustion synthesis

Gang Zheng,[a] Xianli Su,*[a] Tao Liang,[a] Qiangbing Lu,[a] Yonggao Yan,[a] Ctirad Uher,[b] and Xinfeng Tang*[a]

Received (in XXX, XXX) Xth XXXXXXXXX 20XX, Accepted Xth XXXXXXXXX 20XX

DOI: 10.1039/b000000x

The traditional zone melting (ZM) method for fabrication of Bi_2Te_3-based thermoelectric materials has long been considered a time and energy intensive process. Here, a combustion synthesis known as the self-propagating high-temperature synthesis (SHS) is employed to synthesize Bi_2Te_3-based thermoelectric materials. Thermodynamic and kinetic parameters of the SHS process relevant to Bi_2Te_3 and Bi_2Se_3 were systematically studied for the first time. SHS combined with plasma activated sintering (PAS) results in a single phase homogeneous material with precisely controlled composition, no preferential orientation, high thermoelectric performance, and excellent mechanical properties. The technologically relevant average *ZT* value of SHS-PASed $Bi_2Te_{2.4}Se_{0.6}$ from 298 K to 523 K is 0.84, about 25% improvement over the ZM sample. The compressive strength and the bending strength of SHS-PASed $Bi_2Te_{2.4}Se_{0.6}$ are improved by nearly 250% and 30% respectively, compared with those of the ZM samples measured perpendicular to the c-axis. Moreover, the SHS-PAS process is very fast and shortens the synthesis time from tens of hours to 20 min. On account of the simplicity of the process, short synthesis time, minimal use of energy, and scalability of the operation, the SHS-PAS technology provides a new and efficient way for large-scale, economical fabrication of Bi_2Te_3-based compounds.

1. Introduction

With increasing concerns regarding environmental protection and the growing need to use clean energy, thermoelectricity is being explored as an energy conversion technology that might be very useful in a number of applications. Relying on the Seebeck effect to convert heat into electricity and on the Peltier effect to use electrical energy to achieve cooling, such energy conversion processes can harvest waste industrial heat or provide active cooling of electronic devices. Owing to distinct advantages such as an environmental friendliness, vibration-free operation, and exceptionally high reliability, thermoelectric conversion has a potential to impact a wide range of technologies.[1,2] Whether the thermoelectric energy conversion can be commercially successful depends chiefly on two factors. The first one is the conversion efficiency which depends on the material's dimensionless figure of merit *ZT* defined as $ZT=\alpha^2\sigma T/\kappa$, where α, σ, κ, and T are the Seebeck coefficient, the electrical conductivity, the thermal conductivity, and the absolute temperature, respectively.[3] The other factor is whether the high conversion efficiency can be achieved at a competitive cost, certainly the most critical issue for any commercial application.

Bismuth telluride and its alloys with antimony telluride and bismuth selenide have been the primary materials used in thermoelectric energy conversion modules during the past fifty or so years. All three compounds are narrow-gap semiconductors and their appropriate solid solutions are the best room temperature thermoelectric materials.[4,5] Their tetradymite-type crystal structure (space group R-3m) is typified by quintuple sets of parallel layers forming the sequence: -$Te^{(1)}$-X-$Te^{(2)}$-X-$Te^{(1)}$- where X stands for Bi or Sb. In selenides, Te is replaced by Se. The most notable feature of the structure is a weak, van der Waals-type of bonding between the neighboring $Te^{(1)}$-$Te^{(1)}$ (or $Se^{(1)}$-$Se^{(1)}$) layers.[6,7] Commercial forms of p-type and n-type Bi_2Te_3-based materials are typically prepared by zone melting (ZM).[8,9] However, the ZM synthesis requires extensive annealing and it is difficult to control composition precisely. Moreover, the ingot prepared by ZM is highly oriented and cleaves easily due to the already noted weak van der Waals bonding between $Te^{(1)}$-$Te^{(1)}$ layers. Thus, such ingots have poor mechanical properties, their manufacturing cost is high, and they are prone to damage during processing. Although some new synthesis routes have been developed in the recent years, such as ball-milling (BM)-spark plasma sintering (SPS), hot deformation (HP), and melt-spinning (MS)-SPS, these new technologies require specialized equipment and the material often oxidizes and contains impurities.[10-14] Moreover all such existing synthesis methods are energy and time consuming. Therefore, it is of great interest to develop fabrication methods of Bi_2Te_3-based materials that are simple, inexpensive, accomplished in a short period of time, control the composition precisely, and yield samples with high thermoelectric performance and robust mechanical properties.

Self-propagating high-temperature synthesis (SHS) is a method which makes use of exothermic chemical reactions that are self-propagating once initiated. In the past, the SHS synthesis

was used to prepare high temperature refractory, intermetallics, and ceramic materials. In all these cases, the adiabatic combustion temperature T_{ad} (the highest temperature the material reaches during the SHS synthesis) was over 1800 K. This led to an understanding that the self-propagating nature of SHS requires at least 1800 K to proceed.[15-18] Of course, most of the existing thermoelectric materials would decompose at such high temperatures and this is why the technique was not tried to synthesize thermoelectric materials.

Most recently, our team has shown[19,20] that the SHS synthesis can be applied to a wide range of thermoelectric materials and, in this study, we illustrate its versatility on a technologically important case of Bi_2Te_3-based materials. We systematically study the key parameters governing the SHS processing of Bi_2Te_3 and Bi_2Se_3. We wish to note right here that the sister compound, Sb_2Te_3, cannot be prepared by the SHS process on account of the adiabatic temperature being lower than the melting point of the lower melting point elemental constituent, i.e. the reaction is not self-propagating.[19] We show that the SHS process followed by PAS takes merely 20 minutes and results in precisely controlled composition, no obvious preferential orientation, high thermoelectric performance, and excellent mechanical properties. The SHS-PAS technology provides a new and economical way for large-scale fabrication of Bi_2Te_3-based compounds for thermoelectric applications.

2. Experiment

Commercial high purity powders of 99.99% Bi (under 200 mesh), 99.999% Se (under 200 mesh) and 99.99% Te (under 200 mesh) were used as raw materials. The powders with the stoichiometry of $Bi_2Te_{3-x}Se_x$ (x=0-1) were weighed, and then mixed uniformly in an agate mortar for 15 min in air. After the mixed powders were cold-pressed into a pellet using a steel die in air, the pellet was sealed in a quartz tube under vacuum. The SHS process was initiated by heating the bottom of the pellet to the ignition temperature with hand torch. Once ignited, move away and turn off the hand torch. The combustion wave can be sustained by the heat released by the reaction and passed through the whole pellet in several seconds. The product after SHS was ground into powder, and then sintered under the pressure of 30 MPa at 753 K in vacuum using the PAS apparatus[21,22]. The heating rate was 100 K min^{-1} and the holding time at 753 K was 5 min. PAS processing resulted in disk-shaped samples with the diameter of 15 mm and the height of 10 mm. In addition, using the identical SHS-PAS synthesis, we also prepared a sample of $Bi_2Te_{2.4}Se_{0.6}$ with the diameter of 20 mm and the height of 10 mm for measurements of mechanical properties. A ZM ingot with the composition of $Bi_2(Te_{0.93}Se_{0.07})_3$ +0.08 wt% TeI_4 was provided by the Thermonamic Electronics Corp.[23] For measurements of mechanical properties, samples were cut from the ZM ingot with their long axes perpendicular and parallel to the growth direction of the ingot. Thermoelectric properties of the ZM samples were measured along the direction parallel to the growth direction of the ingot, i.e. perpendicular to the c-axis.

Phase identification of the bulk samples was performed by powder X-ray diffraction (PANalytical: Empyrean, Cu Kα). Images of freshly fractured surfaces were obtained by field emission scanning electron microscopy (FESEM, SU8000) with energy-dispersive X-ray spectroscopy (EDS, BRUKER XFlash 6160). Electrical conductivity (σ) and the Seebeck coefficient (α) were simultaneously measured by commercial equipment (ZEM-3, Ulvac Riko, Inc.) under a low pressure of inert gas (He) from 298 K to 523 K. The thermal conductivity (κ) was calculated from the measured thermal diffusivity (D), specific heat (C_p), and density (d) using the relationship $\kappa=DC_pd$. The thermal diffusivity was determined by the laser flash diffusivity method using a Netzsch LFA 457 system, and the specific heat (Cp) was measured by a Thermal Analysis DSC Q20 instrument. All measurements were performed in the temperature range from 298 K to 523 K in the same direction. The density of the bulk samples was measured by the Archimedes method. The relative densities of obtained bulk samples are higher than 98.0%. The Hall coefficient (R_H) and the electrical conductivity (σ_H) at low temperatures from 10 K to 300 K were measured by a Quantum Design measurement system (PPMS-9) with the magnetic field strength of 1 T. The corresponding carrier concentration (n) and carrier mobility (μ_H) were calculated by the following equations: $n=1/eR_H$ and $\mu_H=\sigma/ne$. The combined uncertainty in the determination of ZT based on all measurements involved is ~20%. The compressive and bending strength of the SHS-PAS samples and the ZM ingots were measured using a MTS Systems Corporation, model MTS-E44.104. The size of measured samples was 6 × 3 × 3 mm^3 for the compressive strength and 15 × 2 × 2 mm^3 for the bending strength. The average of 8 samples was used to evaluate the compressive and bending strengths.

3. Results and Discussion

3.1 Thermodynamic and kinetic study of SHS for Bi_2Te_3 and Bi_2Se_3 compounds

Figure 1 shows different combustion stages of the SHS process applied to the Bi_2Te_3 compound. After igniting the compacted powder of Bi and Te at one end, the reaction becomes self-sustained provided the heat released in the chemical reaction is high enough to ignite the neighboring layers of the ingot. In the case of our 18 mm long cylindrical compact, the combustion wave passed through the entire pellet in 3 seconds. The propagation speed of the combustion wave in Bi_2Te_3 was therefore 6 mm s^{-1}, within the range of reported values of 1-150 mm s^{-1}, indicating that the phenomenon is a typical SHS process.[17] A classical criterion for the self-propagating nature of the SHS process states that the adiabatic combustion temperature T_{ad} must reach at least 1800 K.[17,18] According to Eq.1, T_{ad} of Bi_2Te_3 is calculated to be about 860 K, where ΔH_{298} is the enthalpy change in the reaction: $2Bi + 3Te \rightarrow Bi_2Te_3$.

$$\Delta H_{298} = \int_{298}^{T_{ad}} C_p \mathrm{d}T \qquad (1)$$

Clearly, 860 K is much lower than 1800 K. How come Bi_2Te_3 can be synthesized by SHS when its adiabatic temperature is so low? We have shown recently[19] that the classical criterion based purely on the SHS synthesis of high temperature refractory materials is inadequate and should be replaced by a new criterion that specifies that the adiabatic temperature T_{ad} must be larger than the melting point of the lower melting point constituent element. Very simply, the reaction will be self-propagating provided the heat released melts the lower melting point element in which the

other constituent element rapidly dissolves. In the case of Bi_2Te_3, the calculated adiabatic temperature of 860 K as well as the highest measured temperature of 722 K which the sample reaches (see below) are well above the melting point of Bi of 544 K, hence the reaction is self-sustaining. The reason why the highest measured temperature on the compact when the combustion wave passes through is lower than the calculated T_{ad} is due radiation and conduction losses of heat from the reaction zone to the surroundings.

Figure 2(a) shows the temperature profile at the surface of the Bi-Te and Bi-Se compacts as the combustion wave passes through. A thermocouple was set at the center of the mixed powder compact and the temperature profile was recorded once the SHS reaction was ignited. The combustion temperature reached on Bi_2Te_3 is 722 K while for Bi_2Se_3 it is a bit higher at 740 K. The calculated adiabatic temperature for Bi_2Se_3 using Eq.1 is 995 K. The measured propagation speed of the combustion wave in Bi_2Se_3 is faster (8 mm s^{-1}) than in Bi_2Te_3. The black curve in Fig. 2(b) shows the DSC signal with the heating rate of 10 K min^{-1} to 750 K for the Bi-Te mixed powder compact with the Bi_2Te_3 stoichiometry. The red curve is the corresponding signal obtained for the Bi-Se mixed powder compact with the Bi_2Se_3 stoichiometry. There are two endothermic peaks and two exothermic peaks on the DSC trace of Bi_2Te_3. The endothermic peak around 544 K corresponds to the melting temperature of Bi and the other tiny endothermic peak around 685 K corresponds to the eutectic temperature of Te and Bi_2Te_3. Turning the attention to the exothermic peaks, the one near 630 K represents the formation of intermediate phases of BiTe or Bi_4Te_3, and the sharper peak at 688 K corresponds to the formation of Bi_2Te_3. We are certain about these endothermic and exothermic events because we carried out careful XRD measurements on the heated Bi-Te mixed powder compact having the stoichiometry of Bi_2Te_3. The compact was heated in turn to temperatures of 523 K, 573 K, 623 K, 673 K, 723 K, and 773 K with the heating rate of 10 K min^{-1}, and XRD scans were collected at each temperature, see Fig. 2(c). When heated to 523 K and 573 K, the compact remained a mixed powder of Bi and Te. Heating to temperatures of 623 K and 673 K resulted in intermediate phases of BiTe and Bi_4Te_3. A single phase of Bi_2Te_3 was obtained when the mixed powder was heated to 723 K and 773 K. The results give us the confidence to assign the exothermic peak near 630 K to the formation of intermediate phases of BiTe and/or Bi_4Te_3 and the peak at 688 K to the formation of Bi_2Te_3. We interpret the DSC scans as indicating that the SHS synthesis of Bi_2Te_3 is a solid-liquid reaction and proceeds as follows: Te dissolves in molten Bi and forms intermediate phases BiTe and Bi_4Te_3. Subsequently, Te combines with the intermediate phases and forms Bi_2Te_3. In comparison to Bi_2Te_3, the DSC scan of Bi_2Se_3 is simpler, indicating just one endothermic peak (melting of Se) and one exothermic peak (formation of Bi_2Se_3). This implies that the SHS process converts Bi and Se powder directly into the desired Bi_2Se_3 compound without any intermediate phases, which is confirmed by XRD patterns shown in Figure 2(d).

We also studied the influence of heating speeds on the SHS process in Bi_2Te_3. The mixed powder of Bi and Te with the stoichiometry of Bi_2Te_3 was heated to 703 K with different heating rates of 5, 10, 30, and 50 K min^{-1}, as shown in Fig. 3(a). The volume fraction of the intermediate phase BiTe decreased as the heating rate increased from Fig. 3(b) and a single phase of Bi_2Te_3 was obtained when heated to 703 K with the heating rate of 50 K min^{-1}. Similar conclusions also apply to Bi_2Se_3, as shown in Figures 3(c) and 3(d). The intermediate phase Bi_4Se_3 can be observed when heating to 573 with the heating rate of 5 K min^{-1}. With the heating rate larger than 5 K min^{-1} and heating to 573 K, single phase of Bi_2Se_3 was obtained. As the actual heating rate during the SHS process of Bi_2Te_3 or Bi_2Se_3 is much more than 50 K min^{-1} and the combustion temperature is no less than 703 K, all the above compounds can be prepared as a single phase by SHS. However, for solid state reaction, intermediate compounds cannot be avoided due to very low heating rate, and subsequent long time annealing is needed to obtain the single phase Bi_2Te_3 and Bi_2Se_3. We can conclude that single phase Bi_2Te_3 and Bi_2Se_3 can be obtained by SHS in a very short time on the order of seconds. The SHS process of ternary compound is the combination of Bi_2Te_3 and Bi_2Se_3, as shown in Fig. 2(b) with the blue line.

3.2 Phase composition and microstructure

Phase composition of the product after SHS was characterized by powder XRD presented in Fig. 4(a). All peaks in the XRD patterns can be indexed to a standard card JCPDS # 98-001-5753, indicating that all samples are single phases with the crystal structure of the Bi_2Te_3 compound. This demonstrates that ternary solid solutions $Bi_2Te_{3-x}Se_x$ can be synthesized by SHS in a very short time on the order of seconds. An expanded angular range between 55° and 65° shown in Fig. 4(b) depicts an obvious shift to high angles with the increasing content of Se. The shift is due to a smaller atomic radius of selenium (1.15 Å) compared to tellurium (1.4 Å). This also indicates that Se atoms are being incorporated in the crystal lattice of Bi_2Te_3 to form ternary solid solutions during SHS. The final ternary solid solution remains a single phase structure after PAS, and the relative density of samples is above 98%. The entire synthesis process including the SHS processing and sintering takes about 20 min. In comparison with the traditional ZM method, the synthesis period is thus shortened dramatically from tens of hours to 20 min. Moreover, the SHS is very easy to be scaled up. Hence, SHS-PAS shows a great potential for mass production of $Bi_2Te_{3-x}Se_x$.

The crystallographic orientation of Bi_2Te_3-based materials has a crucial impact on their thermoelectric and mechanical properties.[24,25] The orientation factor F along the crystallographic c-axis ([00l] direction) is defined as

$$F = \frac{P - P_0}{1 - P_0} \quad (2)$$

with

$$P_0 = \frac{\sum I_0(00l)}{\sum I_0(hkl)} \quad (3)$$

and

$$P = \frac{\sum I(00l)}{\sum I(hkl)}. \quad (4)$$

Here I (h k l) is the intensity of the (h k l) peak of the SHS-PAS bulk sample or ZM sample, and I_0 (h k l) is the intensity of the (h k l) peak of the SHS powder.[25,26] The sample has no preferred

orientation when the orientation factor F equals to 0, and is fully oriented when the orientation factor F equals to 1. XRD peak positions for SHS-PAS and ZM samples are shown in Fig. 5(a) from which we calculate the orientation factor using Eqs. 2-4. The surface for XRD measurements of the SHS-PAS sample is chosen perpendicular to the direction of the applied sintering pressure and for the ZM sample the surface is taken parallel to the zone melting direction, i.e. perpendicular to the c-axis. The orientation factor F for $Bi_2Te_{3-x}Se_x$ solid solutions after SHS-PAS is calculated as less than 0.1, corresponding to a very weak or almost no preferential orientation, see Fig. 5(b). The orientation factor is essentially constant for the SHS-PAS solid solutions as the content of Se increases. In contrast, the orientation factor of the ZM sample is 0.977, indicating an almost fully oriented structure. All the above data were confirmed by the microstructure analysis shown in Fig. 6. Figures 6(a) and 6(b) show FESEM images of $Bi_2Te_{2.4}Se_{0.6}$ after SHS-PAS, and in Fig. 6(c) is displayed a FESEM photo of the ZM sample where the imaged surface is perpendicular to the zone melting direction. Obviously, this is a near-single crystalline structure displaying parallel sets of cleavage planes, consistent with the large orientation factor. In contrast, the grain structure of the SHS-PAS sample shows no preferred orientation, see Fig. 6(a). Figure 6(d) shows the distribution of elements in $Bi_2Te_{2.4}Se_{0.6}$ after SHS-PAS. The distribution of Bi, Te and Se is uniform on the micron scale. EDS studies indicate that the actual composition of all SHS-PAS samples is close to the nominal composition, as documented in Table 1. This is the consequence of large heating rates and high combustion temperatures in the SHS-PAS process and follows from DSC data discussed in section 3.1. We conclude that SHS-PAS processing results in $Bi_2Te_{3-x}Se_x$ with uniformly distributed elements and very weak or almost no preferential orientation. Significant preferential orientation would result in a large anisotropy in physical properties, especially the mechanical strength.

3.3 Thermoelectric and mechanical properties

Measurements of the Hall coefficient and the electrical conductivity shown in Figures 7(a) and 7(b) served to obtain the carrier concentration and the carrier mobility from the relations $n=1/eR_H$ and $\mu_H=\sigma/ne$. The carrier concentration of the SHS-PAS samples at 300 K hovers around 5×10^{19} cm^{-3}. In contrast, the carrier concentration of the zone melted sample is only 1.9×10^{18} cm^{-3}, more than an order of magnitude lower than in the case of SHS-PAS samples. The large discrepancy between the carrier densities of the SHS-PAS and the ZM samples is likely due to a highly non-equilibrium nature of the SHS synthesis process that might generate vacancies on the Te (or Se) sublattices that each effectively contributes 2 electrons. It is also possible that a large excess of electrons arises as a consequence of holes being trapped at grain boundaries of the SHS samples. We know for fact that when the ZM sample is pulverized and re-compacted by PAS, its carrier density (electrons) reaches comparable values to the SHS-PAS sample. With the increasing content of Se, there is a slight and monotonic decrease in the carrier concentration of SHS-PAS samples, but the concentration never drops much below 4×10^{19} cm^{-3}. This monotonic decrease may be a consequence of the decreasing number of antisite defect Te_{Bi}, consistent with the literature.[11,27] All samples show a weak temperature dependence of the carrier concentration. The carrier mobility (electrons) of the ZM sample perpendicular to the c-axis is as high as 2605 $cm^2V^{-1}s^{-1}$ at 300 K, while the mobility of SHS-PAS samples is considerably lower and decreases monotonically with increasing x from 214 $cm^2V^{-1}s^{-1}$ down to 126 $cm^2V^{-1}s^{-1}$ due to enhanced alloy scattering, see Table 1. As temperature approaches 300 K, the carrier mobility of the SHS-PAS Bi_2Te_3 has a power law dependence of the form $T^{-3/2}$ indicating the dominance of acoustic phonon scattering. The power law dependence is somewhat weaker as the content of Se increases and alloy scattering becomes more important.

Figure 8 shows the temperature dependence of electrical conductivity and of the Seebeck coefficient. The electrical conductivity, see Fig. 8(a), decreases monotonically with increasing temperature indicating that the structure is a degenerate semiconductor. As the content of Se increases, the electrical conductivity progressively decreases because both the carrier concentration and the carrier mobility become smaller. Seebeck coefficients of all SHS-PAS samples are negative in the entire temperature range covered, see Fig. 8(b), indicating the dominance of electrons in the transport process. With the increasing content of Se, the absolute value of the Seebeck coefficient of SHS-PAS samples initially increases and then decreases, consistent with the literature.[11] The highest Seebeck coefficient of -191 μV K^{-1} is obtained at 448 K with the $Bi_2Te_{2.4}Se_{0.6}$ sample.

Assuming a single parabolic band and scattering dominated by acoustic phonons, we express the Seebeck coefficient and electrical conductivity as:

$$\alpha = -\frac{k_B}{e}\times\left[\left(r+\frac{5}{2}\right)-\zeta_F\right] \qquad (5)$$

$$\sigma = 2e\left(\frac{2\pi m_0 k_B}{h^2}\right)^{\frac{3}{2}} T^{\frac{3}{2}}\left(\frac{m^*}{m_0}\right)^{\frac{3}{2}}\mu\exp(\zeta_F) \qquad (6)$$

where k_B, h, m^*, ζ_F, r, T and m_0 are the Boltzmann constant, Planck constant, effective mass, reduced Fermi level, scattering factor, the absolute temperature and the free electron mass, respectively. Then, the Seebeck coefficient can be written as a function of the natural logarithm of the electrical conductivity in the form:

$$\alpha = -\frac{k_B}{e}\left[C+\frac{3}{2}\ell nT+\ell nU-\ell n\sigma\right] \qquad (7)$$

where C is the scattering factor-related parameter equal to 8.68 + r, and U is the weighted mobility defined as $\mu\left(\frac{m^*}{m_0}\right)^{\frac{3}{2}}$.[28] According to the above equation, for a given material system, the value of $\frac{\partial\alpha}{\partial\ell n\sigma}$ should be equal to $\frac{k_B}{e}$ ~86.2 μV K^{-1}. Figure 9 shows the room temperature Seebeck coefficient of $Bi_2Te_{3-x}Se_x$ samples synthesized by different methods as a function of the natural logarithm of electrical conductivity. For the samples synthesized by the SHS-PAS, the slope is 78 μV K^{-1}. For the samples synthesized by ball milling followed by hot pressing (BM-HP) the slope is 114 μV K^{-1}.[27] For the samples synthesized by melt spinning followed by spark plasma sintering (MS-SPS), the slope is 60 μV K^{-1}.[11] All these values deviate significantly

from the classical result of 86.2 μV K^{-1}. This fact indicates that the carrier effective mass or the carrier mobility μ_H is considerably affected by Se alloying and microstructure. Using the room temperature values of the transport parameters, the carrier effective mass m^* and the Lorenz number L of samples can be calculated assuming a single parabolic band model under relaxation time approximation,[29-32] the values being listed in Table 1. With the increasing content of Se, the carrier effective mass m^* of SHS-PAS samples initially increases and then decreases. The $Bi_2Te_{2.4}Se_{0.6}$ sample attains the largest value of the effective mass of $1.19m_0$, consistent with the change of the Seebeck coefficient.

Figure 10(a) shows the temperature dependence of the thermal conductivity for SHS-PAS samples. As the content of Se increases, the thermal conductivity of SHS-PAS samples decreases. The total thermal conductivity can be divided into three parts: $\kappa=\kappa_L+\kappa_B+\kappa_e$, where κ_L is the lattice thermal conductivity, κ_B is the bipolar thermal conductivity representing the diffusion of electron-hole pairs, and κ_e is the electronic contribution estimated by the Wiedemann–Franz relation $\kappa_e=L\sigma T$ with L being the Lorenz number. Room temperature values of the Lorenz number are given in Table 1. According to the Seebeck coefficient discussed above, intrinsic excitations set in above 400 K for all SHS-PAS samples, hence, the thermal conductivity due to the bipolar effect can be ignored at a room temperature. The Debye temperature θ of $Bi_2Te_{3-x}Se_x$ is around 155 K, hence much lower than the room temperature. Consequently, at room temperature, the scattering of phonons is dominated by Umklapp processes and one expects a linear relationship between the lattice thermal conductivity κ_L and the reciprocal temperature *1/T*. As shown in Fig. 10(c), the difference between the experimental κ-κ_e and calculated κ_L is approximately equal to κ_B (Fig. 10(d)). While the bipolar thermal conductivity κ_B increases with temperature, its contribution to the overall thermal conductivity somewhat decreases as the content of Se increases. This is due to an increase in the band gap with the increasing presence of Se. As a function of the content of Se, see Fig. 10(b), the term κ-κ_e above 420 K decreases monotonically, while κ-κ_e below 420 K first decreases and then increases. The lowest room temperature value for κ_L of 0.63 $Wm^{-1}K^{-1}$ is obtained with the $Bi_2Te_{2.4}Se_{0.6}$ sample, in good accord with the result of Rosi et al.[33] For $Bi_2Te_{3-x}Se_x$ solid solutions, the trend in the lattice thermal conductivity as a function of Se content is due to the mass and size difference between Te and Se. Here we use the theory of Callaway[34] for the lattice thermal conductivity of disordered crystals. Assuming that the grain structure of all $Bi_2Te_{3-x}Se_x$ solid solutions is similar, we only consider Umklapp scattering and point defect scattering as the dominant phonon scattering mechanisms. Then, the ratio of the lattice thermal conductivity of the disordered $Bi_2Te_{3-x}Se_x$ (κ_L) to that of the ordered crystal Bi_2Te_3 (κ_L^P) can be expressed as:

$$\frac{\kappa_L}{\kappa_L^P}=\frac{\tan^{-1}(u)}{u} \qquad (8)$$

where the quantity u is a disorder scaling parameter expressed as $u=3.635\times10^6\theta^{-1/2}(\Omega)^{1/6}\left(\kappa_L^P\right)^{1/2}\Gamma^{1/2}$.[35-37] The average atomic volume Ω of Bi_2Te_3 is 33.68×10^{-30} m^3, and Γ is the disorder scattering parameter that includes mass fluctuation scattering parameter (Γ_M) and strain field fluctuation scattering parameter (Γ_S) expressed as $\Gamma=\Gamma_M+\Gamma_S$[38,39]. The chemical composition of a material can be expressed as $A_{1c1},A_{2c2},A_{3c3},A_{4c4},\cdots,A_{ncn}$, where the A_i are crystallographic sublattices in the structure and the c_i are the relative degeneracies of the respective sites. The compound Bi_2Te_3 has n=2, A_1=Bi, A_2=Te, and c_1=2,c_2=3. In general, there will be several different types of atoms that occupy each sublattice, and the k^{th} atom of the i^{th} sublattice has mass M_i^k, radius r_i^k, and fractional occupation f_i^k. The average mass and radius of atoms on the i^{th} sublattice are $\overline{M_i}=\sum_k f_i^k M_i^k$ and $\overline{r_i}=\sum_k f_i^k r_i^k$, respectively. The average atomic mass is $\overline{\overline{M}}=\frac{\sum_{i=1}^n c_i\overline{M_i}}{\sum_{i=1}^n c_i}$. The mass fluctuation scattering parameter can be expressed by

$$\Gamma_M=\frac{\sum_{i=1}^n c_i\left(\frac{\overline{M_i}}{\overline{\overline{M}}}\right)^2 f_i^1 f_i^2\left(\frac{M_i^1-M_i^2}{\overline{M_i}}\right)^2}{\sum_{i=1}^n c_i} \qquad (9),$$

and the strain field fluctuation scattering parameter as

$$\Gamma_S=\frac{\sum_{i=1}^n c_i\left(\frac{\overline{M_i}}{\overline{\overline{M}}}\right)^2 f_i^1 f_i^2 \varepsilon_i\left(\frac{r_i^1-r_i^2}{\overline{r_i}}\right)^2}{\sum_{i=1}^n c_i} \qquad (10),$$

where ε_i is a phenomenological adjustable parameter for the i^{th} sublattice and normally ranges from 10 to 100. The results are shown in Table 2. Strain field fluctuation scattering is dominant for alloy scattering with Γ_S/Γ_M being almost 10 for SHS-PAS samples. However, the difference between the experimental strain field fluctuation scattering parameter and the theoretically calculated strain field fluctuation scattering parameter becomes larger with the increasing content of Se, especially when the Se content is above 0.6. This may be ascribed to the change in the inter-atomic coupling force as the content of Se increases since the difference in the electro-negativities of Bi and Te is different from that between Bi and Se. The bonding strength increases with the increasing content of Se. As a consequence, the literature data[33,40] and our results (see the inset in Fig. 10) concur that the minimum in the lattice thermal conductivity sets in at a surprisingly low Se content around x = 0.6, rather than at what one would expect the maximum disorder at x = 1.5.

Figure 11(a) shows the temperature dependence of the figure of merit *ZT* for SHS-PAS samples and the ZM sample. *ZT* values of a ZM sample and a sample of $Bi_2Te_{2.4}Se_{0.6}$ from the literature are included for comparison. *ZT* values of the SHS-PAS samples initially increase with temperature and, above about 420 K, turn over and decrease with any further increase in temperature, in good accord with the literature[41,42]. A notable exception is $Bi_2Te_{2.2}Se_{0.8}$ where the *ZT* value peaks at around 460 K and especially Bi_2Te_2Se which indicates an increasing *ZT* even at 520 K. The highest *ZT* value of 0.95 is reached near 423 K with $Bi_2Te_{2.4}Se_{0.6}$, while the maximum *ZT* value of the ZM sample is 0.77 at 373 K, almost the same performance as the data from the literature on the same compound[8]. It should be noted that the *ZT* value of $Bi_2Te_{2.4}Se_{0.6}$ synthesized by SHS-PAS is larger than that

of the ZM sample in the entire range of temperatures, as shown in Fig. 11(a). Moreover, due to its low carrier concentration, the *ZT* value of the ZM sample peaks at a much lower temperature of 360 K and becomes distinctly inferior to the SHS-PAS samples at higher temperatures. The average *ZT* values of samples in the temperature range studied, 298 K - 523 K, are calculated through an integral and the results are shown in Fig. 11(b). The average *ZT* value of the ZM sample is 0.67, while the average *ZT* of $Bi_2Te_{2.4}Se_{0.6}$ is 0.84, about a 25% enhancement compared with the ZM sample.

Mechanical properties are very important for applications of TE materials. Good mechanical properties can better withstand applied stresses and improve the reliability of TE modules. Mechanical properties at room temperature were studied on the SHS-PAS $Bi_2Te_{2.4}Se_{0.6}$ and on the ZM sample. Average values of 8 samples constitute a data point. As shown in Fig. 11, the compressive strength of the ZM sample measured parallel to the c-axis is 14 MPa, while measurements perpendicular to the c-axis yield 30 MPa. In contrast, the compressive strength of 104 MPa was measured for the $Bi_2Te_{2.4}Se_{0.6}$ sample prepared by SHS-PAS. The bending strength of $Bi_2Te_{2.4}Se_{0.6}$ synthesized by SHS-PAS is 70 MPa, comparable with the sample prepared by BM-SPS[43] and nearly 30% higher than the bending strength of the ZM sample measured perpendicular to the c-axis (55 MPa) and much higher than 10 MPa for the bending strength measured parallel to the c-axis, the value also reported in the literature[9,44]. It should be noted that the ZM sample cleaves easily along the plane perpendicular to the c-axis, while the SHS-PAS sample is much stronger due to its randomly oriented grains. The effect of grain size on the yield stress is well known in terms of the Hall-Petch relationship:

$$\delta = \delta_0 + Kd^{-1/2} \quad , \qquad (11)$$

where δ is the yield stress of a material with a grain size d, δ_0 is the yield stress of a single crystalline material and K is the material constant, respectively[45,46]. In other words, the yield stress increases as the grain size decreases, and the compressive strength and bending strength of $Bi_2Te_{2.4}Se_{0.6}$ prepared by SHS-PAS is larger than that of the ZM sample because of the fine grain structure of the former.

4. Conclusions

In this study, we prepared Bi_2Te_3-based solid solutions using the self-propagating high-temperature synthesis. Thermodynamic and kinetic parameters of the SHS process for Bi_2Te_3 and Bi_2Se_3 were systematically evaluated for the first time. SHS combined with PAS has been used to prepare n-type $Bi_2Te_{3-x}Se_x$ solid solutions within the time span of 20 min. The resulting material is a single phase, homogeneous structure with no preferred orientation and possesses high thermoelectric performance and excellent mechanical properties. The SHS-PAS synthesis is much faster than the zone melting process and requires considerably less energy. The method thus potentially greatly reduces the manufacturing cost. $Bi_2Se_{2.4}Se_{0.6}$ obtained by SHS-PAS has the peak $ZT = 0.95$ at 423 K. Moreover, the technologically relevant average *ZT* value from 298 K to 523 K is 0.84, about 25% improvement over the zone melted (ZM) sample. Although yielding a superior thermoelectric performance, the above comparison is actually somewhat unfair to the SHS-PAS samples as no doping was used to optimize their performance. The compressive strength and bending strength of $Bi_2Te_{2.4}Se_{0.6}$ prepared by SHS-PAS are 104 MPa and 70 MPa, respectively, the former being more than 3 times the value of the compressive strength of the ZM sample measured perpendicular to the c-axis while the latter is nearly 30% larger than the bending strength measured in the same direction. On account of its simple process, short preparation time, no reliance on expensive equipment, and low energy needs, the SHS-PAS technology provides a new and economical approach for large-scale fabrication of bismuth telluride-based compounds. We also wish to point out that by substituting a higher content of Se for Te, the cost of this n-type material is marginally lower than for the traditional ~10% Se containing Bi_2Te_3 alloy.

Acknowledgement

We wish to acknowledge support from the National Basic Research Program of China (973 program) under project 2013CB632502, the International Science & Technology Cooperation Program of China (Grant No. 2011DFB60150), the Natural Science Foundation of China (Grant No. 51402222, 51172174) and the 111 Project of China(Grant No. B07040). C. U. and X. T. also acknowledge support provided by CERC-CVC under the Award Number DE-PI0000012.

Notes and references

[a] *State Key Laboratory of Advanced Technology for Materials Synthesis and Processing, Wuhan University of Technology, Wuhan 430070, China. E-mail: suxianli@whut.edu.cn (X. Su), tangxf@whut.edu.cn (X.Tang).*
[b] *Department of Physics, University of Michigan, Ann Arbor, Michigan 48109, USA.*

1 L. E. Bell, *Science*, 2008, **321**, 1457.
2 T. M. Tritt, *Science*, 1999, **283**, 804.
3 G. J. Snyder and E. S. Toberer, *Nat. Mater.*, 2008, **7**, 105.
4 J. R. Drabble and C. H. L. Goodman, *J. Phys. Chem. Solids*, 1958, **5**, 142.
5 H. J. Goldsmid, *J. Appl. Phys.*, 1961, **32**, 2198.
6 S. Nakajima, *J. Phys. Chem. Solids*, 1963, **24**, 479.
7 D. L. Greenaway and G. Harbeke, *J. Phys. Chem. Solids*, 1965, **26**, 1585.
8 J. Jiang, L. D. Chen, S. Q. Bai, Q. Yao and Q. Wang, *Mater. Sci. Eng. B*, 2005, **117**, 334.
9 Y. Zheng, H. Y. Xie, S. C. Shu, Y. G. Yan, H. Li and X. F. Tang, *J. Electron. Mater.*, 2014, **43**, 2017.
10 L. D. Zhao, B. P. Zhang, J. F. Li, M. Zhou, W. S. Liu and J. Liu, *J. Alloys Compd.*, 2008, **455**, 259.
11 S. Y. Wang, W. J. Xie, H. Li and X. F. Tang, *Intermetallics*, 2011, **19**, 1024.
12 W. J. Xie, J. He, H. J. Kang, X. F. Tang, S. Zhu, M. Laver, S. Y. Wang, J. R. D. Copley, C. M. Brown, Q. J. Zhang and T. M. Tritt, *Nano Lett*., 2010, **10**, 3283.
13 B. Poudel, Q. Hao, Y. Ma, Y. C. Lan, A. Minnich, B. Yu, X. Yan, D. Z. Wang, A. Muto, D. Vashaee, X. Y. Chen, J. M. Liu, M. S. Dresselhaus, G. Chen and Z. F. Ren, *Science*, 2008, **320**, 634.
14 L. P. Hu, X. H. Liu, H. H. Xie, J. J. Chen, T. J. Zhu and X. B. Zhao, *Acta Mater.*, 2012, **60**, 4431.
15 A. G. Merzhanov, *Ceram. Int.*, 1995, **21**, 371.
16 A. G. Merzhanov, *Adv. Mater.*, 1992, **4**, 294.
17 J. J. Moore and H. J. Feng, *Prog. Mater. Sci.*, 1995, **39**, 243.
18 J. J. Moore and H. J. Feng, *Prog. Mater. Sci.*, 1995, **39**, 275.
19 X. L. Su, F. Fu, Y. G. Yan, G. Zheng, T. Liang, Q. Zhang, X. Cheng, D. W. Yang, H. Chi, X. F. Tang, Q. J. Zhang and C. Uher, *Nat. Commun.*, 2014, **5**, 4908.

20 T. Liang, X. L. Su, Y. G. Yan, G. Zheng, Q. Zhang, H. Chi, X. F. Tang and C. Uher, *J. Mater. Chem. A*, 2014, **2**, 17914.

21 K. Yamazaki, S.H. Risbud, H. Aoyama and K. Shoda, *J. Mater. Process. Tech.*, 1996, **56**, 955.

22 X.A. Fan, J.Y. Yang, W. Zhu, H.S. Yun, R.G. Chen, S.Q. Bao and X.K. Duan, *J. Alloys Compd.*, 2006, **420**, 256.

23 Thermonamic Electronics Corp., Ltd, No 1129, Gaoxin Road, Torch Hi-Tech Zone, Nanchang, Jiangxi, P. R. China, 330096.

24 Q. Lognoné, F. Gascoin, O. I. Lebedev, L. Lutterotti, S. Gascoin and D. Chateigner, *J. Am. Ceram. Soc*., 2014, **97**, 2038.

25 J. J. Shen, L. P. Hu, T. J. Zhu and X. B. Zhao, *Appl. Phys. Lett.*, 2011, **99**, 124102.

26 Y. Saito, H. Takao, T. Tani, T. Nonoyama, K. Takatori, T. Homma, T. Nagaya and M. Nakamura, *Nature*, 2004, **432**, 84.

27 L. P. Hu, T. J. Zhu, X. H. Liu and X. B. Zhao, *Adv. Funct. Mater.*, 2014, **24**, 5211.

28 X. L. Su, H. Li, Y. G. Yan, G. Y. Wang, H. Chi, X. Y. Zhou, X. F. Tang, Q. J. Zhang and C. Uher, *Acta Mater.*, 2012, **60**, 3536.

29 J. Androulakis, Y. Lee, I. Todorov, D. Y. Chung and M. G. Kanatzidis, *Phys. Rev. B*, 2011, **83**, 195209.

30 G. S. Nolas, J. Sharp and H. J. Goldsmid, *Thermoelectrics: Basic Principles and New Materials Developments*, Springer-Verlag: Berlin, 2001.

31 S. Bhattacharya, R. P. Hermann, V. Keppens, T. M. Tritt and G. J. Snyder, *Phys. Rev. B*, 2006, **74**, 134108.

32 W. S. Liu, Q. Y. Zhang, Y. C. Lan, S. Chen, X. Yan, Q. Zhang, H. Wang, D. Z. Wang, G. Chen and Ren, Z. F. *Adv. Energy Mater.*, 2011, **1**, 577.

33 F. D. Rosi, B. Abeles and R. V. Jensen, *J. Phys. Chem. Solids*, 1959, **10**, 191.

34 J. Callaway and H. C. Baeyer, *Phys. Rev*., 1960, **120**, 1149.

35 B. Abeles, *Phys. Rev.*, 1963, **131**, 1906.

36 E. F. Steigmeier, *Appl. Phys. Lett.*, 1963, **3**, 6.

37 M. Zhou, L. D. Chen, W. Q. Zhang and C. D. Feng, *J. Appl. Phys.*, 2005, **98**, 013708.

38 G. A. Slack, Phys. Rev., 1957, **105**, 829.

39 J. H. Yang, G. P. Meisner and L. D. Chen, *Appl. Phys. Lett.*, 2004, **85**, 1140.

40 H. J. Goldsmid, *Introduction to Thermoelectricity*, Springer-Verlag: Berlin, 2009.

41 L. P. Hu, H. L. Gao, X. H. Liu, H. H. Xie, J. J. Shen, T. J. Zhu and X. B. Zhao, *J. Mater. Chem.*, 2012, **22**, 16484.

42 W. S. Liu, K. C. Lukas, K. McEnaney, S. Lee, Q. Zhang, C. P. Opeil, G. Chen and Z. F. Ren, *Energy Environ. Sci.*, 2013, **6**, 552.

43 L. D. Zhao, B. P. Zhang, J. F. Li, H. L. Zhang and W. S. Liu, *Solid State Sci.*, 2008, **10**, 651.

44 J. Jiang, L. D. Chen, S. Q. Bai, Q. Yao and Q. Wang, *Scripta Mater.*, 2005, **52**, 347.

45 C. E. Carlton and P. J. Ferreira, *Acta Mater.*, 2007, **55**, 3749.

46 Y. Zheng, Q. Zhang, X. L. Su, H. Y. Xie, S. C. Shu, T. L. Chen, G. J. Tan, Y. G. Yan, X. F. Tang, C. Uher and G. J. Snyder, *Adv. Energy Mater.*, DOI: 10.1002/aenm.201401391.

Cite this: DOI: 10.1039/c0xx00000x

www.rsc.org/xxxxxx

ARTICLE TYPE

Figure caption:

Figure 1: Typical images of the mixture powder compact of Bi and Te at different times as the combustion wave passes through.

Figure 2. a) Temperature versus time as recorded by a thermocouple attached to a compact during the SHS processing of Bi_2Te_3 and Bi_2Se_3; b) DSC curves with the heating rate of 10 K min^{-1} recorded from 300 K to 750 K for Bi-Te, Bi-Se and Bi-Te-Se mixed powders; c) XRD patterns obtained on a Bi-Te mixed powder compact heated to 523, 573, 623, 673, 723, and 773 K, respectively with the heating rate of 10 K min^{-1}; d) XRD patterns obtained on a Bi-Se mixed powder compact heated to 523, 573, 623, 673, 723, and 773 K, respectively with the heating rate of 10 K min^{-1}.

Figure 3. a) DSC curves recorded with different heating rates to 723 K for Bi-Te mixed powders; b) XRD patterns obtained on a Bi-Te mixed powder compact heated to 703 K with different heating rates; c) DSC curves with different heating rates to 600 K for Bi-Se mixed powders; d) XRD patterns obtained on a Bi-Se mixed powder compact heated to 573 K with different heating rates.

Figure 4. a) XRD patterns of $Bi_2Te_{3-x}Se_x$ (x=0, 0.15, 0.30, 0.45, 0.60, 1.0) powder synthesized by SHS; b) high-angle XRD patterns (55°-65°).

Figure 5. a) Peak assignment and the orientation factor calculation for $Bi_2Te_{2.4}Se_{0.6}$ and the ZM sample. Black trace: powder of $Bi_2Te_{2.4}Se_{0.6}$ after SHS. Red trace: powder of $Bi_2Te_{2.4}Se_{0.6}$ after SHS-PAS. Blue trace: ZM sample, reflections taken on the a-b plane; b) Relationship between the orientation factor and the content of Se for SHS-PAS processed samples.

Figure 6. a) FESEM of the $Bi_2Te_{2.4}Se_{0.6}$ sample; b) High magnification FESEM of the $Bi_2Te_{2.4}Se_{0.6}$ sample; c) FESEM of the ZM sample; d) Element maps of the SHS-PAS processed $Bi_2Te_{2.4}Se_{0.6}$.

Figure 7. a) Temperature dependence of the carrier concentration for SHS-PAS samples; b) Temperature dependence of the carrier mobility for SHS-PAS samples.

Figure 8. a) Temperature dependence of the electrical conductivity for SHS-PAS samples; b) Temperature dependence of the Seebeck coefficient for SHS-PAS samples.

Figure 9. Experimental values of the Seebeck coefficient measured at room temperature plotted as a function of the natural logarithm of the electrical conductivity for $Bi_2Te_{3-x}Se_x$ synthesized by different methods. The MS-SPS data are from Ref. 11, BM-HP data are from Ref. 27, and SHS-PAS data are this work.

Figure 10. a) Temperature dependence of the thermal conductivity for SHS-PAS samples; b) Temperature dependence of κ-κ_e for SHS-PAS samples; c) Temperature dependence of the lattice thermal conductivity for SHS-PAS samples and the lattice thermal conductivity at room temperature for different Se content (inset); d) Temperature dependence of the bipolar thermal conductivity for SHS-PAS samples.

Figure 11. a) Temperature dependence of *ZT* for SHS-PAS samples and the ZM sample measured parallel to the growth direction, i.e., its long axis being perpendicular to the c-axis; b) The maximum and average *ZT* over the entire temperature range from 298 K to 523 K for SHS-PAS samples and the ZM sample.

Figure 12. Average compressive strength and bending strength of $Bi_2Te_{2.4}Se_{0.6}$ and ZM samples.

Table caption:

Table 1: Hall coefficient R_H, carrier concentration n_H, carrier mobility μ_H, reduced Fermi level ξ_F, carrier effective mass m^*, and the Lorenz constant L at 300 K for $Bi_2Te_{3-x}Se_x$ (x=0-1) compounds and the ZM sample.

Samples	Actual composition	R_H ($10^{-7}m^3C^{-1}$)	n_H ($10^{19}cm^{-3}$)	μ_H ($cm^2V^{-1}s^{-1}$)	α (μVK^{-1})	ξ_F (eV)	m^*/m_0	L ($10^{-8}V^2K^{-2}$)
x=0.00	$Bi_2Te_{3.02}$	-0.97	6.42	214.2	-99.1	2.46	0.81	1.92
x=0.15	$Bi_2Te_{2.87}Se_{0.14}$	-1.06	5.92	184.8	-118.6	1.81	0.95	1.83
x=0.30	$Bi_2Te_{2.72}Se_{0.29}$	-1.14	5.48	165.7	-134.0	1.39	1.06	1.78
x=0.45	$Bi_2Te_{2.56}Se_{0.43}$	-1.26	4.95	147.2	-150.3	1.01	1.16	1.73
x=0.60	$Bi_2Te_{2.40}Se_{0.58}$	-1.50	4.16	141.1	-165.9	0.69	1.19	1.69
x=0.80	$Bi_2Te_{2.19}Se_{0.77}$	-1.56	4.01	138.7	-153.9	0.93	1.04	1.72
x=1.0	$Bi_2Te_{1.98}Se_{0.98}$	-1.63	3.84	126.2	-146.6	1.09	0.94	1.74
ZM	$Bi_2Te_{2.75}Se_{0.21}$	-32.89	0.19	2605.4	-210.9	-0.10	0.23	1.61

Table 2. Lattice thermal conductivity κ_L, disorder scaling parameter u, disorder scattering parameters Γ_M, Γ_S(expt), Γ_S(calc), and the strain field related adjustable parameter for the Te sublattice ε_2.

Compound	κ_L ($Wm^{-1}K^{-1}$)	u	Γ_M	Γ_S(expt)	Γ_S(calc)	ε_2
x=0.00	1.04					
x=0.15	0.83	0.976	0.0024	0.0420	0.0420	72
x=0.30	0.72	1.375	0.0047	0.0835	0.0779	72
x=0.45	0.68	1.495	0.0068	0.0975	0.1079	72
x=0.60	0.63	1.733	0.0087	0.1314	0.1323	72
x=0.80	0.65	1.629	0.0108	0.1130	0.1567	72
x=1.0	0.66	1.584	0.0126	0.1044	0.1723	72

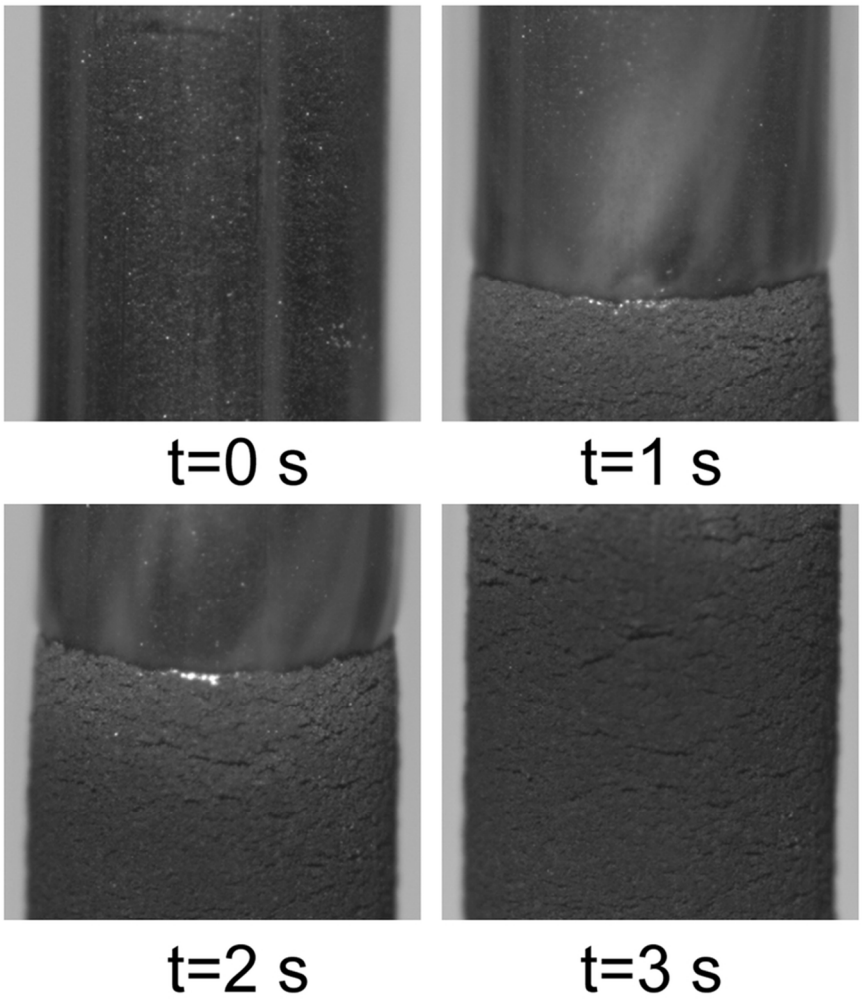

85x90mm (300 x 300 DPI)

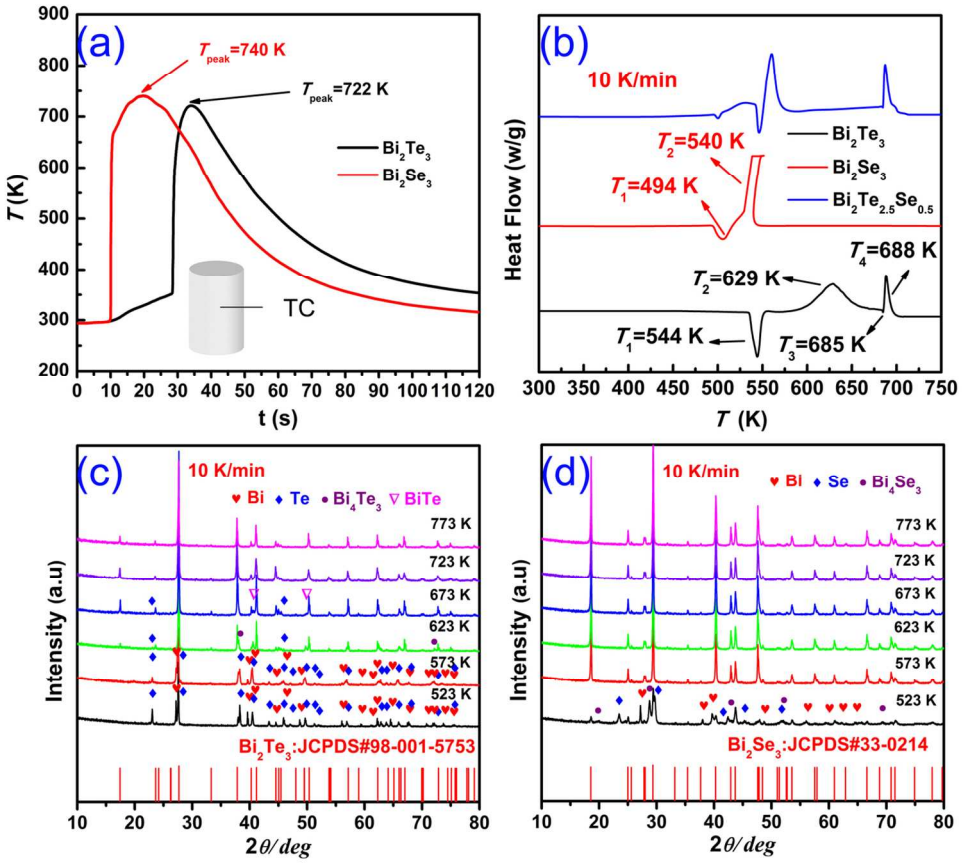

126x114mm (300 x 300 DPI)

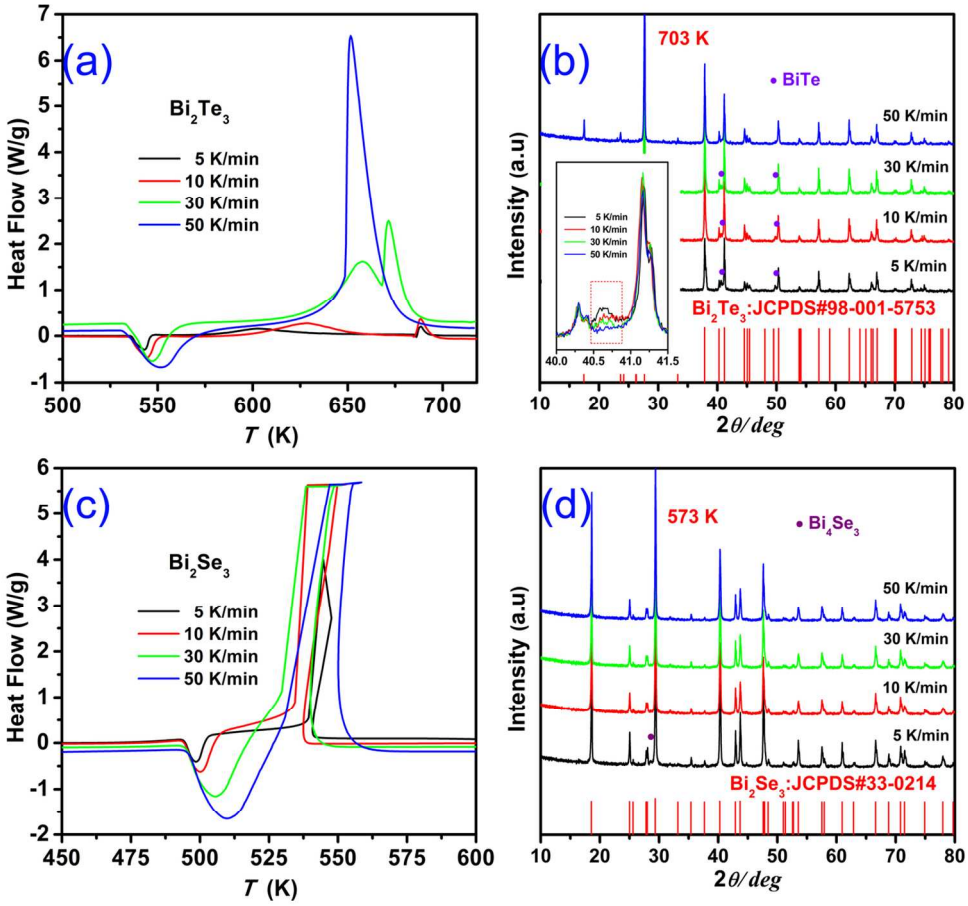

128x117mm (300 x 300 DPI)

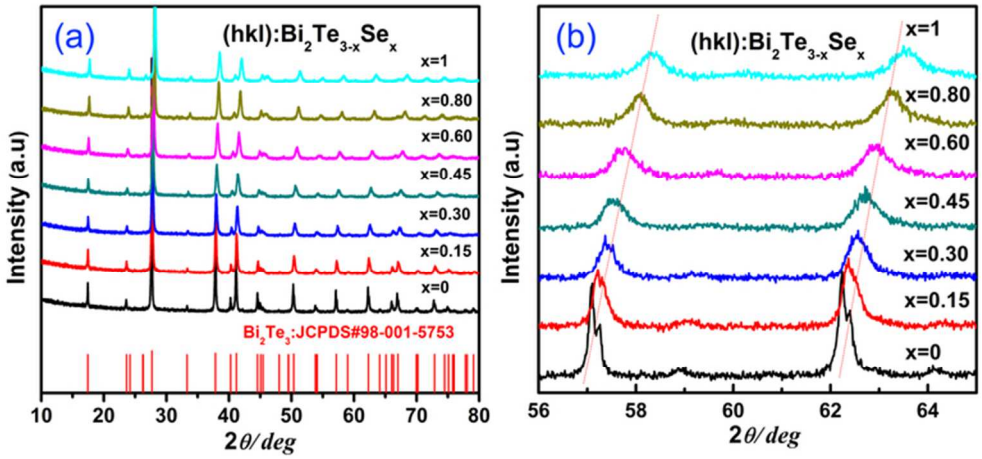

66x31mm (300 x 300 DPI)

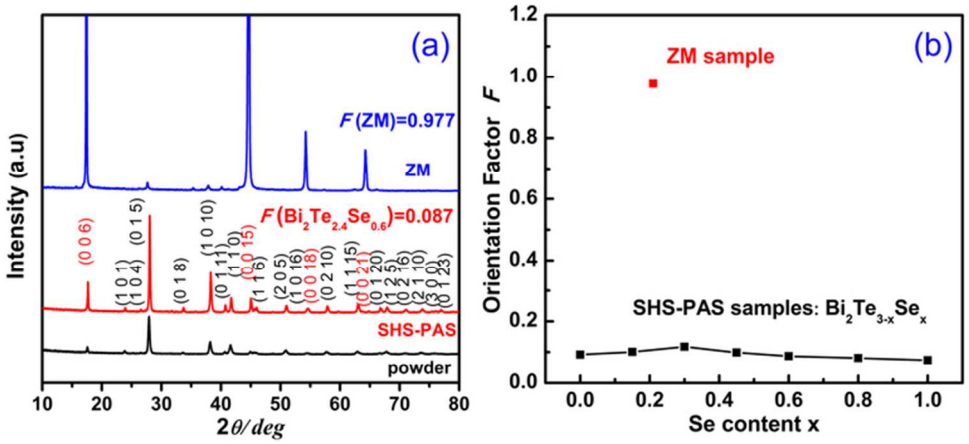

67x32mm (300 x 300 DPI)

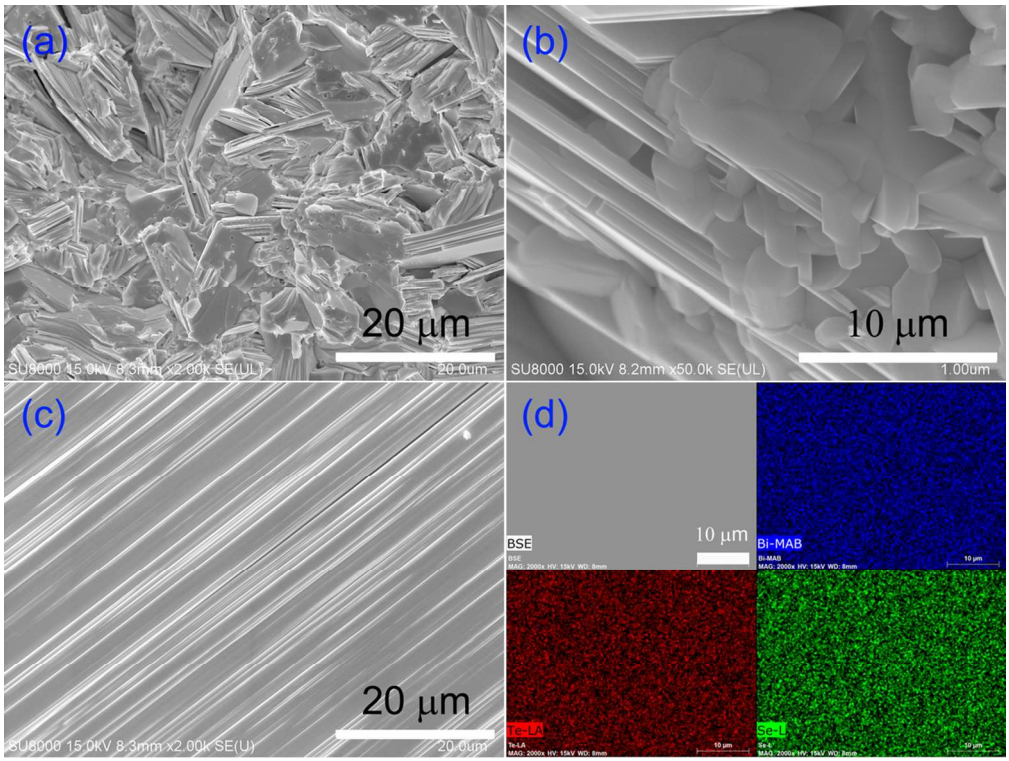

105x79mm (300 x 300 DPI)

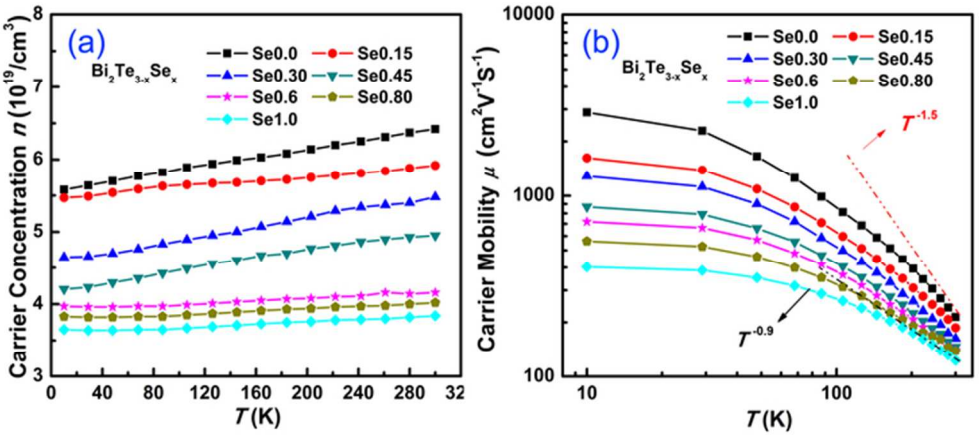

62x28mm (300 x 300 DPI)

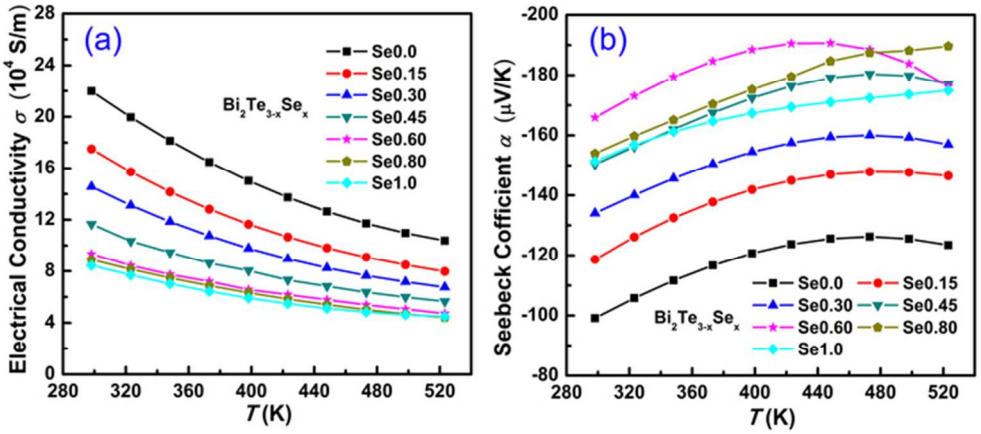

62x27mm (300 x 300 DPI)

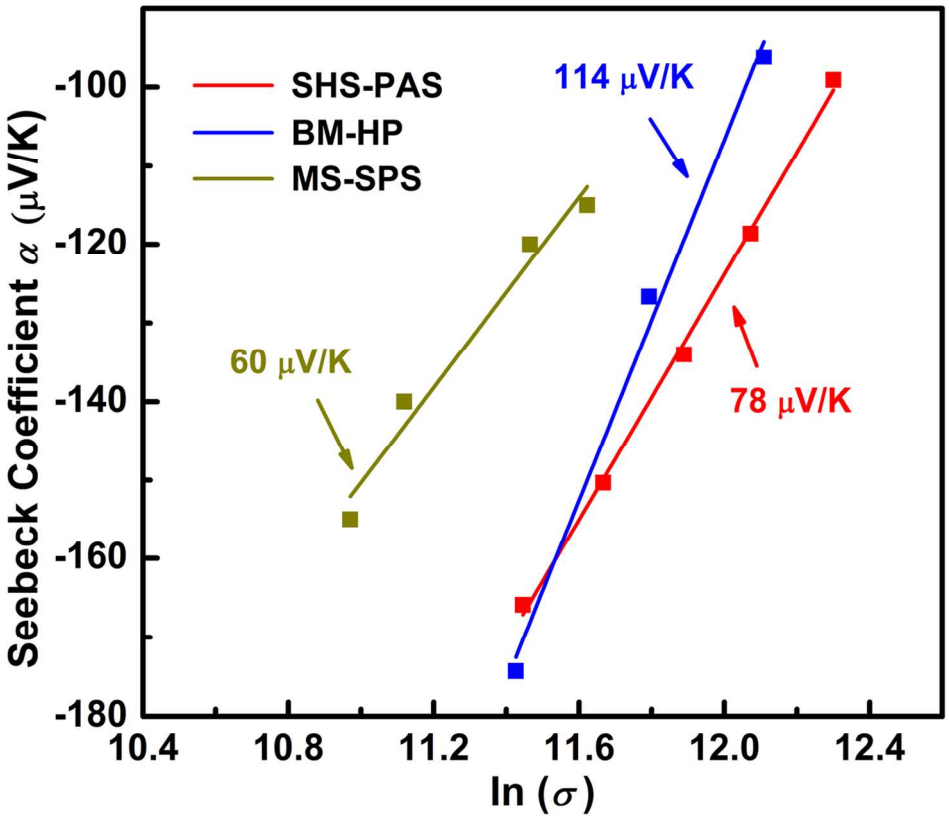

120x103mm (300 x 300 DPI)

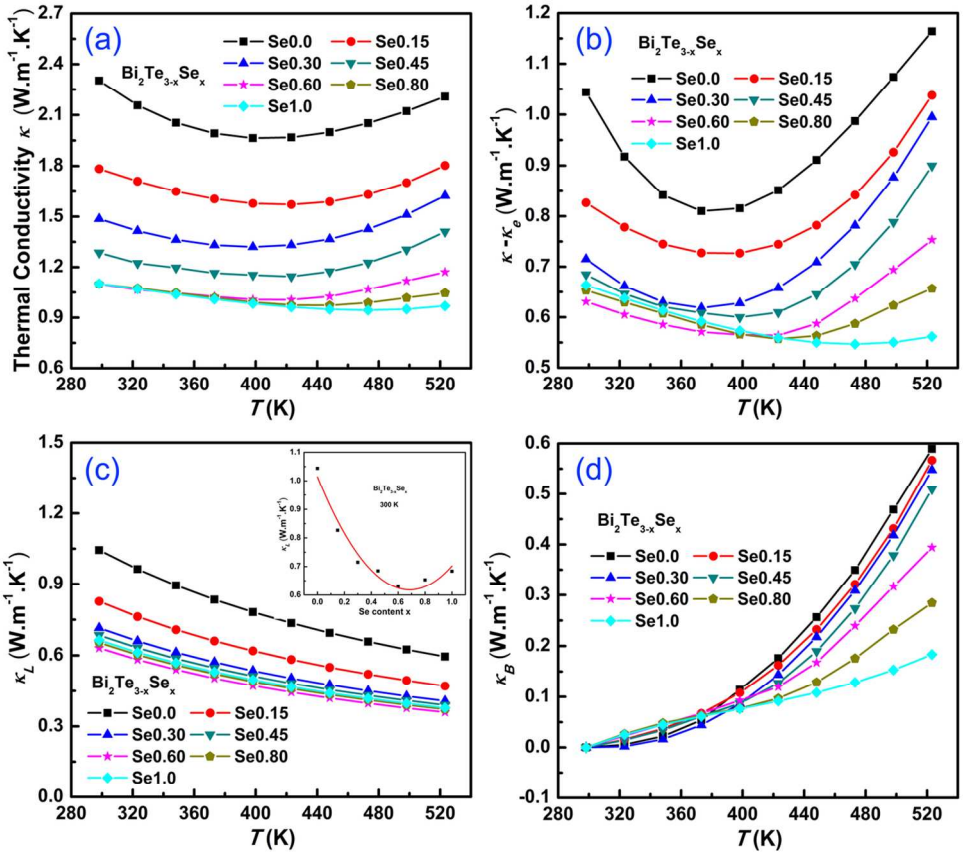

124x110mm (300 x 300 DPI)

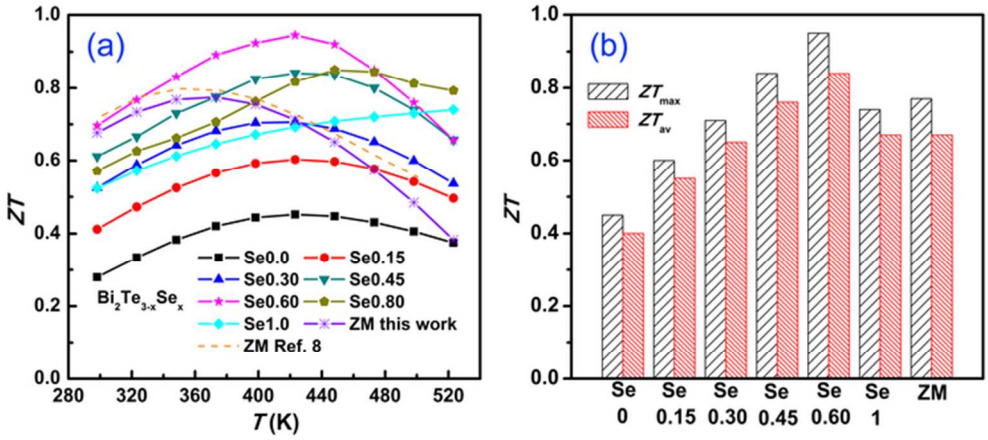

63x29mm (300 x 300 DPI)

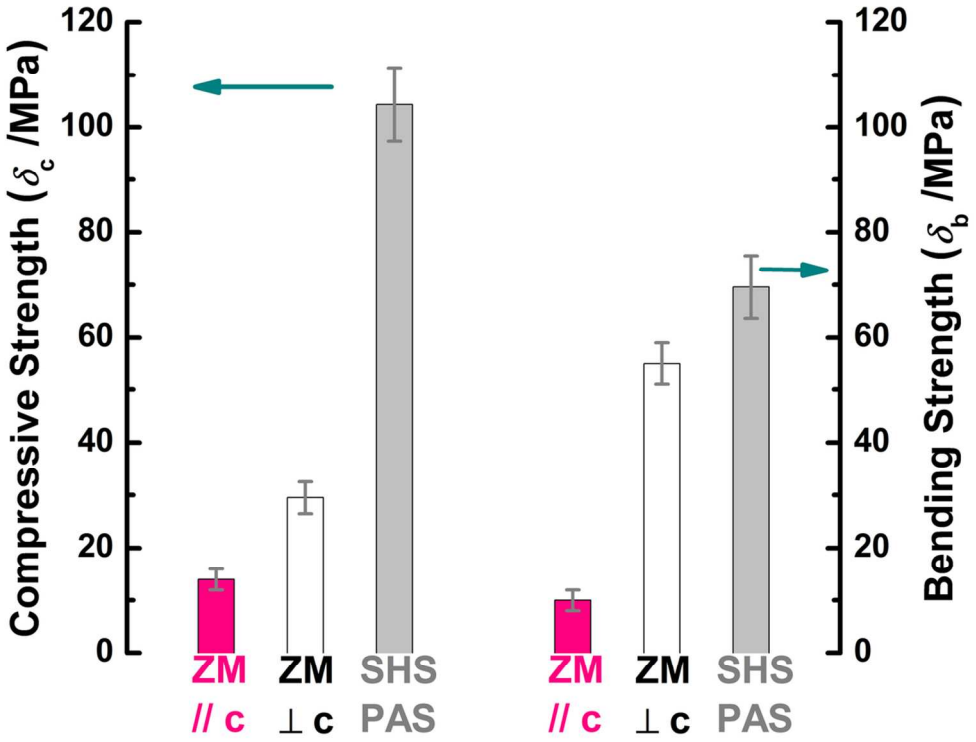

110x87mm (300 x 300 DPI)

Table of content

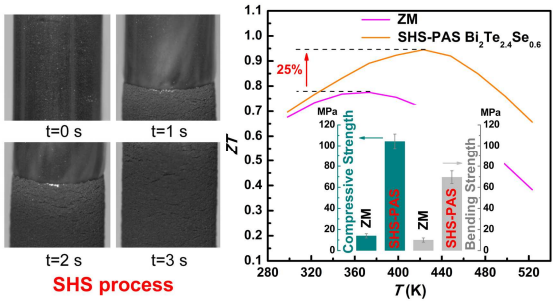

Mechanically robust Bi_2Te_3-based materials with high thermoelectric performance are synthesized by ultra-fast self-propagating high-temperature synthesis in less than 20 minutes.